

# Enhanced Time-Resolved Fourier Transform Infrared Spectroscopic Imaging for Reversible Dynamics

Rohit Bhargava<sup>†</sup> and Ira W. Levin<sup>\*,‡</sup>

Laboratory of Chemical Physics, National Institute of Diabetes and Digestive and Kidney Diseases, National Institutes of Health, Bethesda, Maryland 20892-0520

Received: December 12, 2003

Time-resolved (TR) Fourier transform infrared (FTIR) spectroscopic imaging provides noninvasively spatial and spectral observations of molecular dynamic processes in heterogeneous environments. The technique, however, is limited by the readout time of the imaging focal plane array detector due to a tradeoff between the multichannel detection advantage and the achievable temporal resolution. We describe a generalized implementation of TR-FTIR spectroscopic imaging that, without affecting data quality, allows potential measurements of up to 2 orders of magnitude greater in time resolution than previously reported; that is, time resolutions of milliseconds to tenths of milliseconds are achievable for reversible dynamic processes. As an example, molecular rotations occurring in embedded liquid crystalline microdomains are monitored with a 2.5 ms time resolution allowing an accurate determination of events inherent in the reorientation and relaxation processes.

## Introduction

The focal plane array (FPA) multichannel detection advantage implemented in Fourier transform infrared (FTIR) spectroscopic imaging allows spatially resolved spectral measurements from extended sample areas.<sup>1,2</sup> The large number of detection channels, however, precludes the examination of many dynamic processes as they necessitate longer data acquisition times compared to single-channel detectors. For repeatable, reversible events, time-resolved spectroscopy (TRS) in an imaging modality has recently been introduced<sup>3</sup> to access noninvasively, at the  $\sim 10$  ms time scale, observations of dynamical processes in heterogeneous materials whose characteristic times are of the order of hundreds of milliseconds.<sup>4</sup> This time resolution limitation is currently governed by the rate of snapshot acquisition, or frame rate, of the FPA, which, therefore, defers the study of faster dynamical events until the next generation of array detectors becomes available. The origin of the lengthy time interval between signal sampling by the FPA, or low frame rate, arises from the extended time required to record intensity values for every pixel.<sup>5</sup> A schematic diagram of the typical data acquisition process for IR FPA detectors is shown in Figure 1. The frame time, which is the smallest period between the initiation of successive measurements of the signal, is largely composed of a readout time during which accumulated detector signals are transferred to digital storage. The interval during which the data are actually acquired is the integration time, which is usually small compared to the frame time. For example, the FPA employed in the present study has a minimum frame time of  $\sim 9$  ms and a typical integration time of 0.05 ms. In this paper, we present a generalized implementation of TR spectroscopic imaging that overcomes the limitations imposed by the frame rate and, instead, allows temporal resolutions to be determined by the integration time alone. For current FPA

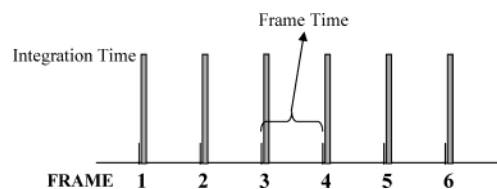


**Figure 1.** A typical data acquisition cycle for a focal plane array detector.

detectors, this represents an improvement of two orders in magnitude compared to previous approaches to TRS imaging.

**Approach to Faster TRS Imaging.** The implementation proposed here utilizes a step-scan infrared interferometer to modulate radiation, a multichannel FPA detector, and custom synchronization electronics, as described in the Experimental Section. A mirror in the interferometer is stepped rapidly and held at a specific position resulting in a constant optical retardation. The mirror is sequentially moved to achieve successive retardations, as shown in Figure 2, for recording the interferogram one resolution element at a time. At every optical retardation, molecular reorientations are initiated within the liquid crystalline microdomains in the composite with the resulting infrared intensity being recorded as a function of time over the field of view of the array detector. As a result, a series of interferograms, corresponding to a specific spatial area on the sample and to specified intervals of time with respect to the initiation of the dynamic event, are obtained. These interferograms are then reorganized into imaging data sets registered to a specific time period in the life of the event. The individual data sets are Fourier transformed and processed to yield absorbance profiles as a function of time.

If the time period between successive temporal measurements at any optical retardation is large, the response to the stimulus may not be sampled correctly, resulting in the observed absorbance profile incorrectly characterizing the underlying physical process. For example, Figure 2 shows three equal sampling intervals of the same response profile denoted by dark

\* To whom correspondence should be addressed.

<sup>†</sup> Fax: 301-496-0825. Phone: 301-496-6847. E-mail: rohitb@niddk.nih.gov.

<sup>‡</sup> Fax: 301-496-0825. Phone: 301-496-6844. E-mail: iw1@helix.nih.gov.

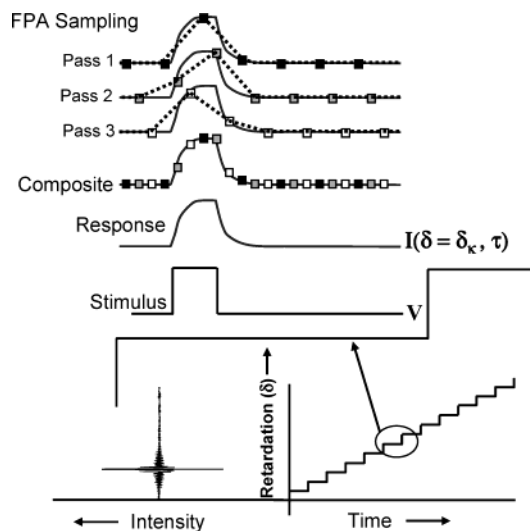


**Figure 2.** The interferogram is obtained, in the step-scan mode, by observing the magnitude of signal at a constant retardation. In step-scan time-resolved spectroscopy, cyclic events are excited by a stimulus and the intensity of the interferogram as a function of time is recorded for every optical retardation. The characteristic profile of fast events may be measured by stimulating multiple times to obtain a composite profile that contains a sufficient number of measurements to reproduce accurately the response.

filled, shaded, and unfilled squares. Depending upon the initiation of data acquisition with respect to the initiation of the molecular process, different profiles indicated by dashed lines are obtained for the three cases. Clearly, none of the three accurately reproduce features of the response curve. If the time period, however, between recording intensities and initiating the process is varied multiple times in a known manner, acquisitions of the same response are temporally offset from each other, resulting in a number of sequentially offset temporal profiles of the same event. A higher temporal resolution than that achieved by any of the single sampling processes is obtained by interleaving the individual profiles into a composite response. The resulting curve from merging the three individual profiles, shown in Figure 2, provides an accurate measurement of the response to the applied stimulus. This multiple pass approach is relevant to any time-resolved spectroscopy method where the time between signal observations is large compared to the time that the signal is measured. The key in any implementation following this procedure is to apply a detection scheme with precise control when the detector accumulates charge in response to the continuous incident radiation. For example, in providing an electronic shutter at the time the signal is acquired, the temporal limits of detection become controlled by the detector and not by the digitization electronics or electronic storage steps.

We employ this method to study a class of polymer composites, termed polymer dispersed liquid crystals (PDLCs),<sup>6,7</sup> whose light transmission properties can be controlled by applied electrical potential differences, making them attractive candidates for electrooptical devices.<sup>8–13</sup> Structurally, these materials contain microdomains, consisting primarily of low molecular weight and electrically responsive LC molecules, embedded in a polymeric matrix. Upon application of an electric field, molecular reorientation is induced with cylindrically shaped molecules, liquid crystals with negative dielectric anisotropy in this case, aligning in the direction of the applied field. Since these molecules are rigid, any molecular species aligned along the long axis of the molecular cylindrical envelope is also aligned in the direction of the applied field. In the experimental configuration that we report here, the electric field is applied

in the direction of transmission of radiation through the sample plane. The absorbance depends on the angle between the long axes of the molecules and the electric field, which changes during the reorientation and relaxation processes. Thus, the absorbance decreases as the molecule orients along the electric field and recovers when the field is removed. Direct observations of localized molecular dynamics from applied electrical fields provide improved correlations of PDLC properties, morphology, and chemical structures, thus allowing an appropriate modeling of these systems.<sup>14</sup>

## Experimental Section

**Instrumentation.** The instrumentation employed consists of three major units: a step-scan spectrometer incorporating a Michelson interferometer, an IR microscope incorporating a large format  $256 \times 256$  IR FPA, and interfacing electronics. A commercially available step-scan spectrometer (Bruker Optics, IFS-66/s) and an all-reflective microscope employing Cassegrainian focusing optics (Bruker IR Scope II) were interfaced in-house to a Mercury Cadmium Telluride (MCT) FPA (Santa Barbara Focalplane, CA). All experiments were carried out in a transmittance mode, using a  $15\times$  objective corresponding to a sample area of  $\sim 750 \times 750 \mu\text{m}^2$ . A single interferogram is acquired for every pixel resulting in a data set of 65 536 interferograms for every time-resolution element. The data are spatially subset to include the central core of high illumination consisting of  $150 \times 150$  pixels to maximize the signal-to-noise ratio. The FPA is equipped with a long wavelength band-pass filter ( $0\text{--}3950 \text{ cm}^{-1}$ ) and an optimized cold shield to prevent aliasing and stray radiation, respectively. Event-locked signal generators (Agilent Inc.) are employed to initiate data acquisition and sample excitation. A commercially available amplifier (Krohn-Hite Corp.) is employed to increase the electrical potential difference generated between 1 and 5 V at 2 kHz and applied to the PDLC with use of a gain factor of 5. All signals were measured with a digital oscilloscope (Tektronics Inc.) to verify signal magnitude and timing.

**Sample.** The PDLC consists of a phase-separated blend of the commonly used liquid crystal eutectic mixture, E7 (EM Industries, Inc.), and a UV-curable adhesive, NOA65 (Norland Optical Adhesive Inc.). E7 consists of four components: 51% *n*-pentylcyanobiphenyl (5CB), 25% *n*-heptylcyanobiphenyl (7CB), 16% *n*-octyloxycyanobiphenyl (8OCB), and 8% *n*-penyltcyanoterphenyl (5CT). The polymeric matrix, NOA65, is reportedly a mixture composed primarily of trimethylolpropane diallyl ether, trimethylolpropane tris thiol, isophorone diisocyanate ester, and a benzophenone photoinitiator<sup>15</sup> of proprietary composition. All materials were used as received. Weight ratios (70% LC) of the two components were mixed at 350 K, a temperature above the nematic-to-isotropic transition of the LC and the critical temperature for the uncured blend. A small amount of the solution is deposited between indium tin oxide (ITO) coated  $\text{CaF}_2$  plates separated by  $10 \mu\text{m}$  diameter cylindrical fiber glass spacers and photocured<sup>16</sup> by using a long-wave UV lamp (UVP Inc.) after maintaining the sample for 4 h at a low temperature ( $-5 \text{ }^\circ\text{C}$ ), as detailed elsewhere,<sup>17</sup> followed by subsequent curing at room temperature.

**Experimental Parameters.** Interferogram data points are acquired at every fourth zero crossing of the He–Ne laser (under a sampling ratio of 4) to limit the acquired data to the detection range of the FPA and to limit the size of the data set. The resulting interferograms, consisting of 1024 points each, are zero filled by a factor of 2 and fast Fourier transformed to provide single beam spectra with a nominal spectral resolution of  $8 \text{ cm}^{-1}$

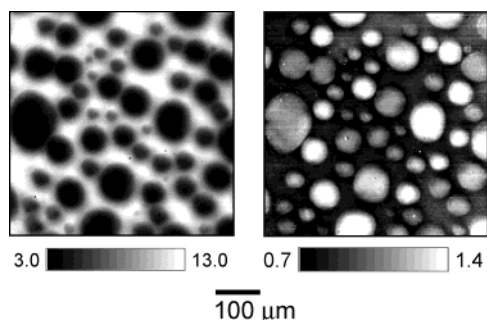


**Figure 3.** Infrared absorbance images for (a) peak area of a polymer-specific carbonyl stretching vibrational mode and (b) peak area of the liquid crystal-specific nitrile stretching vibrational mode.

and 0–3950  $\text{cm}^{-1}$  spectral range. The sample was excited once every 500 ms resulting in a data collection time of  $\sim 510$  s per complete interferogram acquisition. The maximum frame rate of the focal plane array is  $\sim 114$  Hz; hence, the FPA was set to acquire data once every 10 ms (100 Hz). The entire data set was acquired by employing four passes for each excitation voltage with the FPA synchronized to acquire data starting 0.0, 2.5, 5.0, and 7.5 ms after the initiation of molecular reorientation. Forty data points, spaced 10 ms apart, were acquired during each pass for an overall monitoring time of 400 ms, a temporal resolution of 2.5 ms, and data file size of  $\sim 21$  GB. The time required for trigger pulses is  $1 \mu\text{s}$ , which is negligible compared to other times in the collection process.

### Results and Discussion

A multipass approach to generalize time-resolved imaging is implemented for a PDLC whose chemical composition distribution is shown in Figure 3. A plot of the absorbance of the polymer specific carbonyl stretching vibrational mode ( $1735 \text{ cm}^{-1}$ ) demonstrates the phase-separated structure of the com-

posite. Liquid crystalline domains, in which polymer concentration is low, are embedded in a polymer-rich phase. A complementary plot of the absorbance of the liquid crystal specific nitrile stretching vibrational mode ( $2227 \text{ cm}^{-1}$ ) confirms the distributions of the components. Individual droplets of the composite, however, demonstrate different absorbance values for the liquid crystal-specific mode. The absorbance depends on the relative orientation of the transition moment of the vibrational mode and the electric field of the propagating infrared radiation. Hence, the same concentration of LC gives rise to different absorbance values, as average orientations in droplets with respect to the electric vector of the radiation differ and the radiation is slightly polarized due to multiple reflections in the optical train.

Average absorbance profiles from 20 pixels in a droplet are plotted as a function of time in Figure 4a. The time labels next to the four plots indicate the offset times of the individual profiles from the first data acquisition process. Although all profiles are measuring the same process, gross errors result in a description of the characteristic events due to the coarse resolution. The four individual profiles are then interleaved to yield the profile denoted by the open squares in the lowest profile of panel a, Figure 4. The composite profile contains sufficient detail to correctly interpret the dynamic absorbance changes. Specifically, the fast reorientation of the liquid crystal during the first 20 ms is well captured. The visualization of a fast relaxation process during the first  $\sim 10$  ms following removal of the electrical stimulus is also afforded by this higher temporal resolution. The large number of sampling points are, however, not required for the later times in the relaxation when the change is of a smaller magnitude and considerably slower.

The signal-to-noise ratio (SNR) of the profile remains the same for analyzing both rapid molecular changes, which are larger in magnitude but require a greater number of temporal observations to accurately specify, and the slower dynamics near

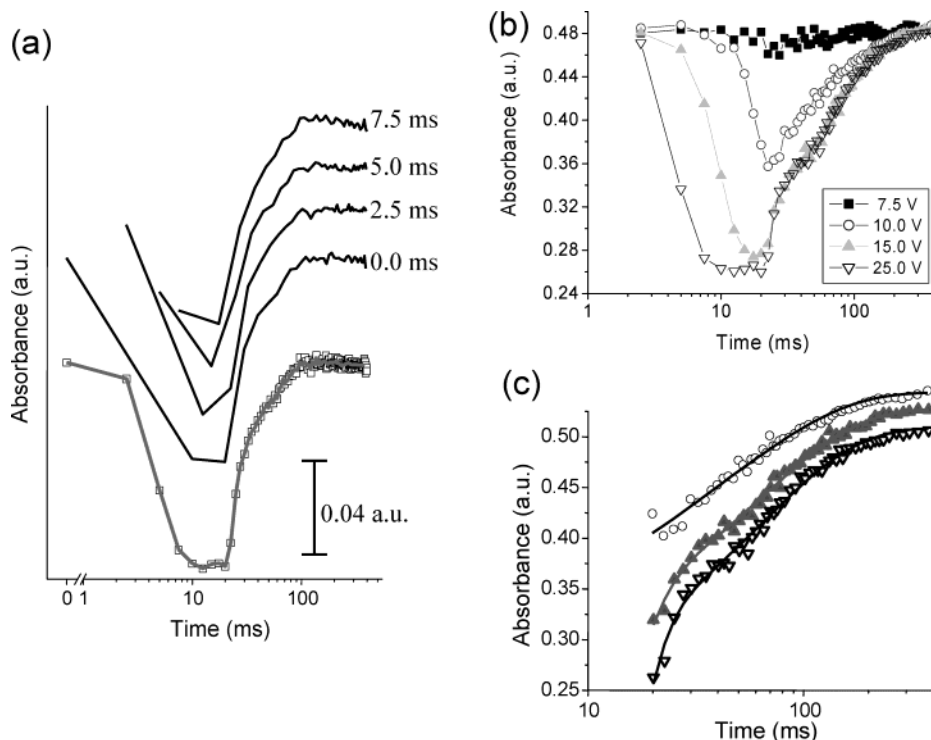


**Figure 4.** (a) Temporal absorbance profiles for four different offsets between the start of data acquisition and initiation of the dynamic event as indicated by the times along the curves. The temporal resolution of each is 10 ms. By interleaving the profiles, a temporal resolution of 2.5 ms can be obtained for the composite. (b) Temporal absorbance profiles for a droplet bulk region as a function of the magnitude of the applied electric field potential. (c) Experimental data and best fit curves with use of a two-process model for the relaxation process.

the end of the process, when higher SNRs are necessary to monitor accurately the smaller changes in magnitude. One approach to enhancing the SNR is to average multiple imaging data sets to obtain a co-addition advantage. Another approach is to selectively co-add pixels to obtain lower noise profiles.<sup>18</sup> The first approach results in increased data acquisition times, larger data sets, and longer processing times, while the increased SNR does not further elucidate the section of the temporal profile where the signal change is large. The second approach degrades image quality and results in the loss of spatial specificity negating some advantages of imaging. Further, locating pixels in precisely the same microenvironments may also be impossible in irregularly distributed heterogeneous structures. A third approach would be to selectively average parts of the temporal profile,<sup>19</sup> or spectra before obtaining the profile, to yield sections of the profile with a higher SNR. For the experiments reported here, the convergence of the slow changes and their low magnitudes makes this an ideal averaging approach. The first 32 points are unchanged, two adjacent points are averaged for the next 32 points to obtain 16, the following 32 points yield 8 by averaging four adjacent points, and so on. The segmentally averaged profile is superimposed on the composite curve indicated by open squares in Figure 4a, demonstrating the lower noise characteristics for the longer time intervals. All subsequently discussed profiles in this paper are obtained by averaging in this manner.

Temporal profiles as a function of the applied potential difference are shown in Figure 4b. For smaller applied voltages (<~7.5 V), there is little change in the absorbance, while for the larger values the changes are a strong function of applied voltage, as reflected in the decreasing absorbance profiles. The relaxation of the initial absorbance is considerably longer than the reorientation process, demonstrating the existence of both fast and slow dynamics. This two-step relaxation is ordinarily theorized to arise from the droplet boundary and the bulk, respectively.<sup>20</sup> In this case, however, the droplet–matrix boundary is more than 10–30  $\mu\text{m}$  away, but the infrared activity of the substrate interface and the droplet are both sampled by the transmitted beam. Hence, the substrate and microdomain bulk likely give rise to two different relaxation modes.<sup>21</sup> Although the slower component of the response is determined by free energy minimized orientations dictated by domain boundary anchoring and defects, the fast relaxation process is due to strong anchoring of molecular layers close to the substrate.

A dual exponential model of the form below can be employed to fit observed data

$$A(t) = A(0) - \Delta A_s \exp\left[-\frac{(t - t_{\text{off}})}{\tau_s}\right] - \Delta A_b \exp\left[-\frac{(t - t_{\text{off}})}{\tau_b}\right] \quad (1)$$

where the absorbance at the start of the experiment,  $A(0)$ , is related to the time the electric field is removed,  $t_{\text{off}}$ , the change in absorbance values,  $\Delta A_s$  and  $\Delta A_b$ , and characteristic times,  $\tau_s$  and  $\tau_b$ , for the substrate and bulk, respectively. The fitted curves for three voltages are shown in Figure 4c and are well-reproduced by the model above. The parameters obtained, after fitting the curves until the reduced  $\chi^2$  was smaller than 0.0002, are summarized in Table 1. The figures indicate the relaxation at 10 V is predominantly a single relaxation process. The faster relaxation process increases in magnitude when the voltage is increased, while the magnitude of change due to the slower relaxation process remains the same for the two cases, also

**TABLE 1: Goodness of Fit and Curve Parameters for Fitting the Relaxation Processes in Figure 4c<sup>a</sup>**

voltage (V)	$\Delta A_s$ (au)	$\tau_s$ (s)	$\Delta A_b$ (au)	$\tau_b$ (s)	$R^2$
10	0.02(0.017)	16.7(15.6)	0.11(0.02)	66(7.6)	0.981
15	0.045(0.005)	4.6(1.1)	0.167(0.003)	67(1.9)	0.993
25	0.063(0.006)	4.0(0.75)	0.167(0.004)	66(1.9)	0.992

<sup>a</sup> The values in parentheses are errors in the determination.

demonstrating the fast mode. The characteristic time constant for the slower relaxation process is the same for all cases, indicating that the same molecular processes occur. The regression coefficient is indicative of the goodness of fit seen in the plots.

The data indicate that the molecules close to the substrate are not reoriented at lower applied fields, as expected from their large anchoring energies on ITO surfaces. The response of the molecules away from the surface saturates at ~12 V and the absorbance change for this component is ~36% of the total absorbance of the pixel. It can be expected that the surface absorbance change may saturate at ~0.08 au when the applied fields are of the order of ~40 V, representing ~15% change in the total absorbance. The difference between the surface layers and bulk is consistent with experiments reported for thin layers<sup>22</sup> and those close to substrates.<sup>23</sup> The fast reorientation process characteristics are in excellent agreement with values reported for thin layers.<sup>22</sup> Images corresponding to different times, obtained using the fitted profiles, for the liquid crystalline domains are shown in Figure 5a–f. Since the absorbance change from the LC vibrational mode in the matrix is typically ~5% (vide infra), the criterion for domain–matrix segmentation is that the absorbance change should be at least 15%. The formation of localized regions of high or low intensity can be seen very quickly. Specifically, by comparing images at all recorded times, regions of high absorbance running across the droplet can be observed from the time the electric field is turned off, as indicated by the arrow in Figure 5d. These features relax slowly and their disappearance is quickly followed by stability in the absorbance values of the domain bulk, as, for example, observed by the region indicated by the arrow in Figure 5e. Domain boundaries, as indicated by the arrow in Figure 5f, appear to stabilize quickly as no changes in the domain boundary regions are discernible after a short time.

In Figure 6, 30–100 pixel-average relaxation profiles for the regions indicated by arrows are shown. Best fit profiles are superimposed to help visualization and demonstrate substantial differences in the relaxation profiles of the different regions of the composite. While the absorbance of the defect changes quite rapidly initially, the subsequent relaxation is long. The domain bulk relaxes in a two-step manner, as previously discussed. The domain boundary pixels relax rapidly at first, completing their relaxation within 100 ms, the fastest process associated with the domain. The fastest relaxation process for the PDLC, however, is in the matrix where the anchoring due to the rigid polymer is strongest and leads to a complete relaxation within ~10 ms. We emphasize that this fast process is in sharp contrast with a previous discussion of this system where the matrix LC relaxation could only be measured at the order of ~100 ms.<sup>3</sup> Here, the LC concentration is lower and the degree of polymerization is higher due to the large curing time, which influences both the matrix relaxation and the relaxation in the domain–matrix interphase. The field of view average clearly does not provide any of these details and is actually misleading in the time taken to achieve constant absorbance (~100 ms). Stabilization of the absorbance implies that the molecular orientation is at equilibrium, and by relying on an average absorbance,

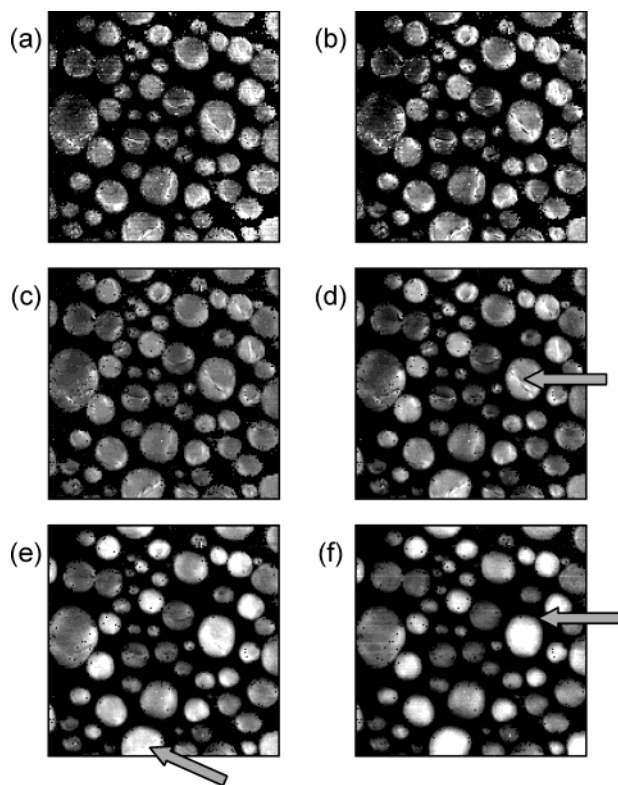


**Figure 5.** The distribution of absorbance for the relaxing PDLC after the applied potential difference (25 V) is removed at (a) 20, (b) 25, (c) 32.5, (d) 45, (e) 95, and (f) 379 ms.

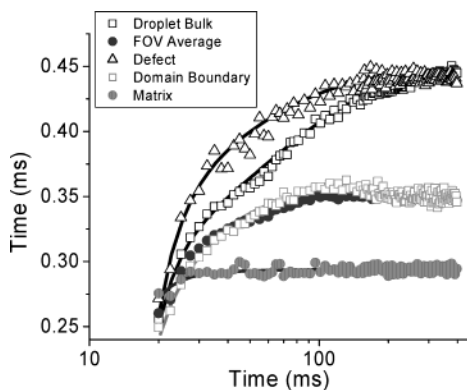


**Figure 6.** Average absorbance profiles during the relaxation of orientation for the different regions indicated in parts a–f in Figure 5. The best fit lines are superimposed for all except the average of the field of view (FOV).

significant nonlinear hysteresis effects would arise for a film is driven at a different voltage after the 100-ms interval. A more appropriate time period between changes in applied stimuli would be based on the complete relaxation of the droplet bulk ( $\sim 500$  ms). The removal of electric field is followed first by relaxation of molecules close to the substrate and then by relaxations at domain boundaries. Defect structures relax next, inducing recovery in the bulk regions of the microdomains. Thus, the sequence and relative time scales for all events can be determined accurately by using FTIR spectroscopic imaging.

In a previous study,<sup>3</sup> where PDLCs were formed with use of the same materials by a different method and higher LC concentrations, the relaxation process was found to be at least four times longer than the one reported in the current paper. Hence, we implemented a four-pass method to achieve a temporal resolution of 2.5 ms. There is an uncertainty of  $\sim 25$   $\mu$ s in initiation of data acquisition by the FPA, but by

implementing, for example, a 100-pass approach, a 100- $\mu$ s time resolution is attainable. Clearly, design and implementation of an automated clock to time the pulse for initiating each pass with respect to the stimulus-initiating pulse would be required, although this does not present a technological limitation. A further reduction in the time between temporal sampling can be achieved by decreasing the integration time, which, unfortunately, serves to reduce the SNR of the acquired spectral data. In consideration of the detector's SNR characteristics and electronic uncertainty in the measurements, a temporal resolution greater than  $\sim 100$   $\mu$ s cannot likely be achieved.

In summary, we have implemented a multipass approach in generalizing TRS imaging, in which the entire experiment is repeated with the timing scheme reset once per interferogram acquisition, thus enabling time resolutions of milli- to submilli-seconds. A more efficient approach, however, is to employ a programmable timing sequence to excite the sample repeatedly at every optical retardation in the same interferometer mirror sweep, which will result in an efficiency improvement of  $\sim 10\%$  compared to the current implementation. The current implementation, however, has the advantage of smaller individual data sets that allow for more convenient and faster data processing and storage.

## Conclusions

A generalized implementation of time-resolved infrared spectroscopic imaging, which allows for higher temporal resolutions to be accessed, is reported. A simultaneous averaging benefit can arise for systems in which multiple processes exist with slow changes occurring over longer time scales. This paper extends the temporal resolution close to the millisecond domain from the 10-ms domain. Extension to the submillisecond domain, while being cumbersome, can nevertheless be accomplished without extensive hardware changes. All important events in the reorientation and relaxation of liquid crystalline domains are clearly observed, allowing molecular relaxations at substrate and domain boundary layers, within defect structures and within the microdomains to be distinguished by their characteristic time scales.

## References and Notes

- (1) Lewis, E. N.; Treado, P. J.; Reeder, R. C.; Story, G. M.; Dowrey, A. E.; Marcott, C.; Levin, I. W. *Anal. Chem.* **1995**, *67*, 3377–3381.
- (2) Lewis, E. N.; Gorbach, A. M.; Marcott, C.; Levin, I. W. *Appl. Spectrosc.* **1996**, *50*, 263–269.
- (3) Bhargava, R.; Levin, I. W. *Macromolecules* **2003**, *36*, 92–96.
- (4) Bhargava, R.; Levin, I. W. *Appl. Spectrosc.* **2003**, *57*, 357–367.
- (5) Bhargava, R.; Levin, I. W. *Anal. Chem.* **2001**, *73*, 5157–5167.
- (6) Doane, J. W.; Vaz, N. A.; Wu, B. G.; Zumer, S. *Appl. Phys. Lett.* **1986**, *48*, 269–271.
- (7) Drzaic, P. S. In *Liquid Crystal Dispersions*; World Scientific: Singapore, 1995.
- (8) West, J. L. *Mol. Cryst. Liq. Cryst.* **1988**, *157*, 427–441.
- (9) Doane, J. W. In *Liquid crystals—applications and uses*; Bahadur, B., Ed.; World Scientific Publishing: Singapore, 1990; Vol. 1.
- (10) Blanca, C. M.; Gutierrez, R. C.; Domingo, Z. B. *Mol. Cryst. Liq. Cryst.* **2001**, *368*, 4023–4030.
- (11) Chidichimo, G.; Formoso, P.; Manfredi, S.; Favaro, G.; Mazzucato, U.; Romani, A. *J. Appl. Phys.* **2001**, *90*, 4906–4914.
- (12) Lucchetta, D. E.; Manni, A.; Karapinar, R.; Gobbi, L.; Simoni, F. *Mol. Cryst. Liq. Cryst.* **2002**, *375*, 397–409.
- (13) Bouteillier, L.; LeBarny, P. *Liq. Cryst.* **1996**, *21*, 157–174.
- (14) Aloe, R.; Chidichimo, G.; Golemme, A. *Mol. Cryst. Liq. Cryst.* **1991**, *202*, 9–24.
- (15) Smith, G. W. *Mol. Cryst. Liq. Cryst.* **1991**, *196*, 89–102.

- (16) Bhargava, R.; Wang, S.-Q.; Koenig, J. L. *Macromolecules* **1999**, *32*, 8982–8988.
- (17) Bhargava, R.; Wang, S.-Q.; Koenig, J. L. *Macromolecules* **1999**, *32* (8), 2748–2760.
- (18) Bhargava, R.; Ribar, T.; Koenig, J. L. *Appl. Spectrosc.* **1999**, *53*, 1313–1322.
- (19) Rodig, C.; Siebert, F. *Appl. Spectrosc.* **1999**, *53*, 893–901.
- (20) Mei, E.; Higgins, D. A. *J. Chem. Phys.* **2000**, *112*, 7839–7847.
- (21) Toriumi, H.; Akahane, T. *Jpn. J. Appl. Phys.* **1998**, *37*, 608–612.
- (22) Noble, A. R.; Kwon, H. J.; Nuzzo, R. G. *J. Am. Chem. Soc.* **2002**, *124*, 15020–15029.
- (23) Leyte, J. C.; Jesse, W.; Leyte-Zuiderweg, L. H.; van Woerkom, P. C. M. *J. Phys. Condens. Matter* **1998**, *10*, 11617–11626.